

MULTIBAT: Unified workflow for fast electrochemical 3D simulations of lithium-ion cells combining virtual stochastic microstructures, electrochemical degradation models and model order reduction

Julian Feinauer^a, Simon Hein^{b,c}, Stephan Rave^f, Sebastian Schmidt^e, Daniel Westhoff^{a,*}, Jochen Zausch^e, Oleg Iliev^{e,g}, Arnulf Latz^{b,c,d}, Mario Ohlberger^f, Volker Schmidt^a

^a*Institute of Stochastics, Ulm University, Helmholtzstr. 18, 89069 Ulm, Germany*

^b*Institute of Engineering Thermodynamics, German Aerospace Center (DLR), Pfaffenwaldring 38-40, 70569 Stuttgart, Germany*

^c*Helmholtz Institute for Electrochemical Energy Storage (HIU), Helmholtzstraße 11, 89081 Ulm, Germany*

^d*Institute of Electrochemistry, Ulm University, Albert-Einstein-Allee 47, 89081 Ulm, Germany*

^e*Fraunhofer Institute for Industrial Mathematics ITWM, Kaiserslautern*

^f*Applied Mathematics, Center for Nonlinear Science & Center for Multiscale Theory and Computation, University of Münster, Einsteinstr. 62, 48149 Münster, Germany*

^g*Institute of Mathematics and Informatics, Bulgarian Academy of Science, Sofia, Bulgaria*

Abstract

We present a simulation workflow for efficient investigations of the interplay between 3D lithium-ion electrode microstructures and electrochemical performance, with emphasis on lithium plating. Our approach addresses several challenges. First, the 3D microstructures of porous electrodes are generated by a parametric stochastic model, in order to significantly reduce the necessity of tomographic imaging. Secondly, we integrate a consistent microscopic, 3D spatially-resolved physical model for the electrochemical behavior of the lithium-ion cells taking lithium plating and stripping into account. This highly non-linear mathematical model is solved numerically on the complex 3D microstructures to compute the transient cell behavior. Due to the complexity of the model and the considerable size of realistic microstructures even a sin-

*Corresponding author

Email address: daniel.westhoff@uni-ulm.de (Daniel Westhoff)

gle charging cycle of the battery requires several hours computing time. This renders large scale parameter studies extremely time consuming. Hence, we develop a mathematical model order reduction scheme. We demonstrate how these aspects are integrated into one unified workflow, which is a step towards computer aided engineering for the development of more efficient lithium-ion cells.

Keywords: Stochastic 3D microstructure modeling, Lithium plating, Lithium stripping, Electrochemical simulation, Model order reduction

1. Introduction

The ubiquity and importance of rechargeable lithium-ion batteries lead to the increasing demand for physics-based simulation methods that are able to analyze and predict battery behavior. These methods can not only contribute in
5 improving cell design and operation, but they can also greatly support battery research in its understanding of basic mechanisms, like lithium plating that determine battery life and safety, which is yet not well understood.

The electrochemical simulation of lithium-ion cells goes back to the work of Newman and his co-workers [1, 2, 3]. Their simulation methodology is based
10 on the porous electrode theory developed by Newman [4]. This model approach neglects the details of electrode microstructures and describes them as a homogeneous medium where electrolyte and the solid material coexist at every point. The most commonly used model of Newman only considers the through-direction of the battery. It takes into account the diffusion of lithium ions into
15 the active material by assuming a spherical, microscopic particle of average size in each discretization point in which a one-dimensional diffusion equation is solved. Hence this model is sometimes called a pseudo-2d (P2D) model [5]. There exist many applications for Newman-type models like the study of cell behavior as well as degradation [5, 6, 7, 8]. But the main drawback of these
20 models is that the complex electrode microstructures are only approximately accounted for by a few aggregated parameters: the thickness of the electrode L ,

the porosity ε , the mean particle radius r and the specific interface area between electrolyte and active material a [1]. Furthermore, *effective* transport parameters need to be determined to account for the influence of the microstructure on the *average* species transport. While these models are able to describe the average battery behavior surprisingly well [8, 9, 10, 11], they cannot be expected to capture local microscopic effects. In particular, many degradation effects like, for instance, lithium plating depend on the local environment. Hence homogenized models cannot fully capture the interplay between microstructure and degradation phenomena with sufficient predictive power. Therefore, more fundamental, spatially resolved models should be applied that are able to take the electrode microstructure explicitly into account [12, 13]. Without simplifications like volume averaging for the P2D-models these allow the computation of quantities on the scale of the electrode microstructure and are hence better suited for plating predictions. To give an example, in [14] a microstructure-based simulation study for a LCO-graphite battery was performed concentrating on the discharge behavior for a 2D cut of one given realization of the electrodes. Although the numerical solution of these micro-models is computationally much more demanding they have been successfully applied to study cell performance [15, 16, 17], coupling to thermal effects [11, 18, 19], and to account for phase-separation dynamics within certain electrode materials [20]. A framework for these spatially resolved simulations has been implemented in the software BEST [21].

Lithium plating is one of the major degradation factors and security risks in lithium-ion batteries. Lithium plating describes the deposition of metallic lithium on the negative electrode [22]. This causes a loss of usable lithium (which reduces the cell's capacity) and might lead to the growth of lithium dendrites which can eventually create a short-circuit between the electrodes which can favor catastrophic thermal runaways. While model extensions to account for lithium plating are typically based on the porous electrode theory [8, 23, 24, 25, 26] only very little work has been published where lithium plating models take the electrode microstructure into account [27, 28]. In a recent

publication [29] a micro-scale model has been developed that is able to take the inhomogeneous electrode structure into account. The research presented in the
55 current paper is based on this degradation model.

Spatially resolved electrochemical simulations as described above allow investigations of electrochemical behavior for realistic 3D microstructures. Thus, as input for these simulations, realistic 3D image data of battery electrodes is needed, which is already available even in-operando [30]. However, tomographic measurements of battery electrodes in 3D involve high costs and efforts.
60 A methodology that has proven to be very promising in this context is stochastic microstructure modeling. Based on (only one or a few) tomographic measurements, a 3D parametric stochastic microstructure model can be constructed and calibrated using tools from stochastic geometry [31]. The model has been
65 implemented in our software library GEOSTOCH [32]. It is able to describe the complex geometric microstructure in a statistical sense with only a few parameters such that each realization of the model represents the morphological characteristics of the tomographic image data (e.g., the distributions of particle size and shape, pore size distribution, etc.). Once fitted to tomographic image
70 data, with hardly any effort an arbitrary number of realistic 3D microstructures can be generated on the computer. Moreover, systematic variation of model parameters allows the realization of virtual, but still realistic microstructures. Such an approach has been considered, for example, in the context of organic solar cells [33]. Using regression in the parameter space, microstructures that
75 represent various manufacturing conditions could be generated on the computer and analyzed regarding their functionality. This results in an enormous reduction of complexity, as (most of) the structures do not have to be manufactured in the laboratory, but only tomographic image data of a few ones is needed. Similar examples of stochastic microstructure modeling can be found in literature
80 [34, 35, 36]. In this work, a stochastic microstructure model for anodes in lithium-ion batteries [37] is used.

While the aforementioned microscopic battery model can be solved by relatively standard iterative numerical methods, the solution process is compu-

tationally very demanding. In order to get meaningful results a sufficiently
85 large electrode cutout needs to be resolved in the simulation. This results in
huge time-dependent discrete systems which require considerable computing re-
sources, already for single simulation runs. Computational studies to identify
critical parameters, to estimate the dependence of degradation on operating con-
ditions or to support optimal design and control of batteries, however, require
90 many forward simulation runs with varying material or state parameters and are
thus virtually impossible. Hence, model reduction approaches for the resulting
parameterized systems are indispensable for such simulation tasks. Concern-
ing model reduction for lithium-ion battery models, we refer to the pioneering
work [38] in the context of proper orthogonal decomposition (POD), and to the
95 more recent contributions [39, 40, 41, 42, 43, 44, 45] in the context of reduced
basis methods. In the work presented here, we rely on an implementation of
recent model reduction methods (such as the reduced basis method, POD, and
the empirical interpolation method) implemented in our model order reduction
library pyMOR [46, 47].

100 The ability to efficiently and realistically predict the degradation behavior
(here: lithium plating) of lithium-ion batteries under arbitrary load conditions
relies on the following prerequisites:

1. A physics-based predictive microscopic battery model that includes the
plating mechanism.
- 105 2. A method to create a number of virtual, yet realistic microstructures as
basis to understand the correlation between structural properties and bat-
tery performance and degradation behavior.
3. A numerical method that is able to efficiently perform a considerable num-
ber of three-dimensional, microstructure-resolving simulations for a vari-
110 ety of operating conditions.
4. A software interface that is able to integrate these aspects into a common
workflow.

Within the project MULTIBAT [48] the authors developed and technically implemented a workflow that covers all the aforementioned aspects, namely
115 stochastic geometry generation, model extension to account for plating, numerical implementation and development of model order reduction techniques. There are numerous papers in the literature (including several ones written by the authors of the present paper) on different components of the presented workflow. However, we are not aware of any publication on an algorithm inte-
120 grating all these components into one single, holistic workflow, which enables comprehensive solutions of really complex problems related to Li-ion batteries. Thus, development, implementation, and testing of a holistic algorithm / workflow which integrates all components of the above-mentioned chain is one of the main contributions of the present paper. A feasibility study for a really complex
125 problem, such as plating, is presented in order to illustrate the capabilities of the workflow that has been developed. The investigation of the interplay between 3D microstructure and electrochemical processes during the plating processes, which up to our knowledge has not been done so far in the literature, is another main contribution of the present paper.

130 The authors' developments on the individual components of the workflow have been reported earlier, details can be found in the references listed in the present paper, hence, these components are presented here relatively shortly. The emphasis in the present paper is given to the developed interfaces, to the integration of all the components into one single workflow, to the peculiarities
135 related to the selected feasibility study, and to the parametric study of the plating process in stochastic geometry generation. Special attention is paid to computational efficiency, adapting the model reduction approach to the heavily nonlinear system of partial differential equations. The presented study reveals, that the complex information produced by the interplay between microstruc-
140 ture, lithium-ion transport and intercalation kinetics is hidden in a vastly reduced subspace of the full 3D information contained in the time-dependent scalar fields for lithium-ion concentration and electrochemical potential. The essential dynamics leading to plating in a complex microstructure can be repre-

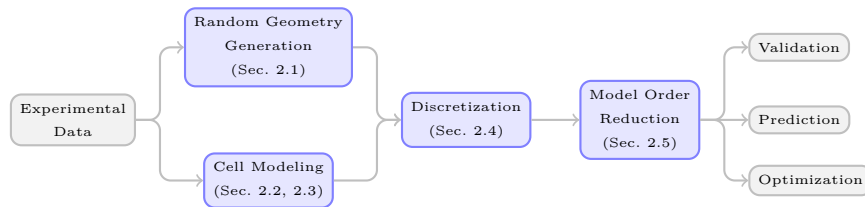


Figure 1: Schematic overview of the MULTIBAT workflow.

sented by a sophisticated reduced model without losing spatial precision. The
 145 advantage of the model presented in this paper is the ability to perform fully 3D
 microstructure-resolved simulations of plating with nearly the same numerical
 efficiency as simulation with a P2D model i.e. a 1D volume averaged battery
 model, in which all structural details are lost. We report on the MULTIBAT
 workflow and briefly describe the details of all the individual aspects in Sec-
 150 tion 2. In Section 3 we demonstrate the application of the developed methods
 by showing and discussing results of a simulation study and conclude with a
 summary in Section 4.

2. The MULTIBAT workflow

In this section we discuss the individual components of the MULTIBAT
 155 workflow (see Fig. 1) and their realization in more detail. Based on experi-
 mental data, random electrode geometries with the same or modified structural
 characteristics are generated (Sec. 2.1), and a mathematical model of the rel-
 evant electrochemical effects is formulated (Sec. 2.2 and 2.3). The resulting
 continuum model is then discretized (Sec. 2.4) and reduced (Sec. 2.5), leading
 160 to a quickly computable microscale model of the cell dynamics on realistic elec-
 trode geometries. The software implementation and integration into a unified
 modeling and simulation workflow is discussed in Sec. 2.6.

It should be noted that, while we present a specific realization of the MULTI-
 BAT workflow targeted at lithium plating, the same workflow can be applied
 165 to other questions in electrochemistry and similar problem domains. Each in-

dividual component can be further developed and optimized for other specific applications, independently of the other workflow components.

2.1. Generation of random structures

The study of local effects in the complex microstructures of battery anodes
170 by spatially resolved models is computationally very expensive, particularly re-
garding random access memory. Therefore, only quite small sample sizes can
be considered. As we are interested in local phenomena, there is a need for
high-resolution of the images, which on the other hand means that the images
typically only represent small cutouts of the material. This is why, in order to
175 get reliable results, the computer experiments have to be carried out repeatedly
using different samples. Furthermore, the imaging techniques are complex in
preparation and involve long imaging times as well as high costs. This is why a
suitable approach is to use randomly generated images of microstructures using
parametric stochastic 3D models. This approach has already been used success-
180 fully in related applications for energy materials in fuel cells [49] and solar cells
[33]. A parametric stochastic model which describes the spatial structure is de-
veloped for the material and its parameters are fitted to image data. Using the
calibrated model, an arbitrary number of structures that are similar to the im-
age data in a statistical sense can be generated with hardly any effort. ‘Similar
185 in a statistical sense’ means that the realizations of the model do not resemble
the image data exactly, but with respect to aggregated quantities and spatial
properties. For example, simple characteristics like volume fraction and specific
surface area can be matched, but also more complex spatial characteristics like
the distribution of pore sizes or local tortuosity. Thus, realizations of a para-
190 metric stochastic microstructure model are an ideal input for spatially resolved
electrochemical simulations. A further advantage is that their parameters can
be changed to create virtual structures that have not been produced in the lab-
oratory yet, and the electrochemical performance of those virtual structures can
be analyzed on the computer, a procedure called virtual materials testing.

195 Here, we make use of a parametric stochastic 3D microstructure model for

anode structures from lithium-ion battery cells [37]. Besides the validation based on structural characteristics [37] a validation using spatially resolved electrochemical simulations has been performed [50]. The variability of the modeling approach used here is demonstrated since the same model with some adaptations
 200 can be used to generate microstructures for energy cells [37] and power cells [51].

We now briefly recall some details of the stochastic 3D model that is used to generate the virtual anode microstructures used in the MULTIBAT workflow. As mentioned above the model has already been published [37] and all parameters as well as further details can be found there. Generally, the construction
 205 of the model consists of four steps that are also depicted in Fig. 2.

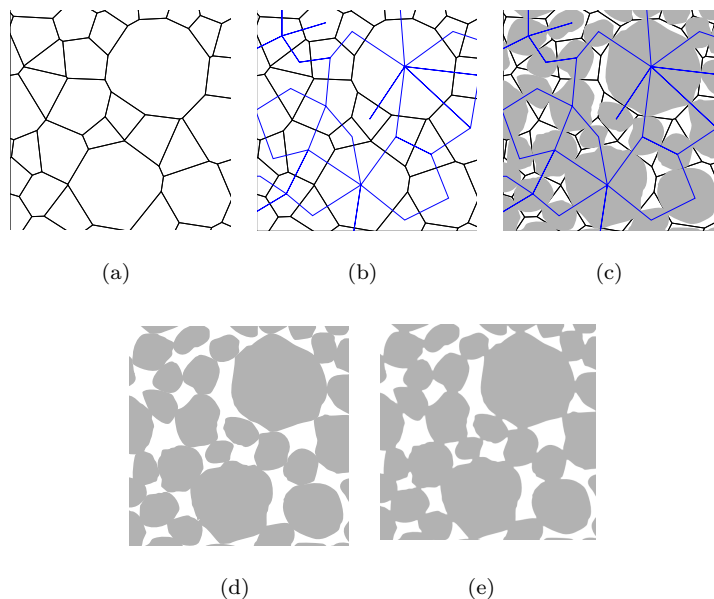


Figure 2: Schematic depiction of the stochastic model. (a) A random tessellation is produced, which roughly determines the particle shapes, sizes and locations. (b) A random graph describes how the particles are connected to each other. (c) The connected particles are generated using random fields on the sphere. (d) and (e) The connected particles are retained and morphological smoothing is carried out. Reprinted from [37] with permission from Elsevier.

First, the locations, sizes and shapes of the particles are determined. Tech-

nically speaking, a Laguerre tessellation is generated (see Fig. 2(a)) based on a random sequential adsorption process. This tessellation decomposes the region
 210 of interest into convex polytopes. Later on, a particle is placed inside each of these polytopes. Thus, the Laguerre tessellation roughly indicates the spatial arrangement of particles. For details regarding tessellations, a broad spectrum of literature is available [31, 52, 53, 54].

In the next step, a connectivity graph is generated that describes which
 215 particles are supposed to be connected, i.e., for each polytope P , we determine a set of neighboring polytopes $\{P_i, i = 1, \dots, N\}$, $N \in \mathbb{N}$. The particles that are placed inside $\{P_i, i = 1, \dots, N\}$ have to touch the particle in P . Full connectivity of all particles is ensured by the usage of a minimum spanning tree [55]. Further connections are added to the minimum spanning tree depending on the size
 220 of the facet between two polytopes, as the probability of two particles being connected is larger for larger facet areas. Such a graph is depicted in Fig. 2(b).

Now, a particle can be realized in each polytope, fulfilling the boundary conditions, i.e., touching the particles indicated by the connectivity graph. In more detail, the particles are modeled using Gaussian random fields on the
 225 sphere. Thus, the shape of the particles can be characterized by a mean radius μ and the angular power spectrum $A : [0, \infty) \rightarrow [0, \infty)$, see [56]. The angular power spectrum is approximated by the function $A(l) = \frac{al+b}{l^2+cl+d}$ with coefficients $a = 0.4241$, $b = 0.356$, $c = -3.858$ and $d = 3.903$. In more detail, we do not use the mean radius μ directly but we generate the particles in a way that
 230 their volume is proportional to the volume of corresponding Laguerre cells. The particles are sampled with the boundary conditions indicated by the connectivity graph using a special sampling algorithm that creates only realizations of the given Gaussian random field that fulfill those conditions.

The schematic depiction in Fig. 2(c) shows the particles with the tessellation
 235 and the connectivity graph. One can clearly see that the particles touch each other where indicated by the graph and on the other hand also fill their respective Laguerre polytopes. Fig. 2(d) shows the system of connected particles without the tessellation and the connectivity graph as these are auxiliary tools

that are no longer needed after the creation of particles.

240 Finally, a morphological smoothing [57] is performed on the system of connected particles to mimic the effect of binder. In the given sample the volume fraction of the binder as well as the contrast in the tomographic images were too low to identify and model the binder as separate phase. From the known production process (slurry coating) we assume that this approach produces a
245 similar effect as depicted in Fig. 2(e).

In Fig. 3(a) and 3(b), a cutout from the tomographic image data can be compared to a simulated anode structure. A very good visual accordance can be observed.

The model described so far is an excellent tool to generate virtual anode microstructures of energy cells, which are characterized by a high volume fraction
250 of the solid phase. However, note that it can not directly be used to model the morphology of anodes in power cells, because due to the lower volume fraction of the solid phase, the boundary conditions for particles cannot be fulfilled reasonably. Therefore, an extension of the model has been proposed [51]. To account
255 for the lower volume fraction, a Laguerre tessellation with marked polytopes is used. The polytopes are marked either as ‘filled’, i.e., a particle is placed in the polytope, or as ‘empty’, which means that no particle is placed here. Thereby, a reasonable allocation of the different polytopes as well as full connectivity of the resulting structure is ensured. Furthermore, the model is able to include
260 anisotropy effects of the solid phase, i.e., particles can be elongated in horizontal direction rather than in vertical direction. This results in a remarkable flexibility such that the model can be used to create a broad spectrum of virtual anode microstructures with a variety of morphological properties, see Fig. 3(c) for some examples.

265 In this study, we focus on electrochemical simulations of anode microstructures in energy cells. Thus, all microstructures which are discussed in the present paper, are created using the energy cell model [37]. Electrochemical simulations on virtual structures generated by the power cell model are subject of further research.

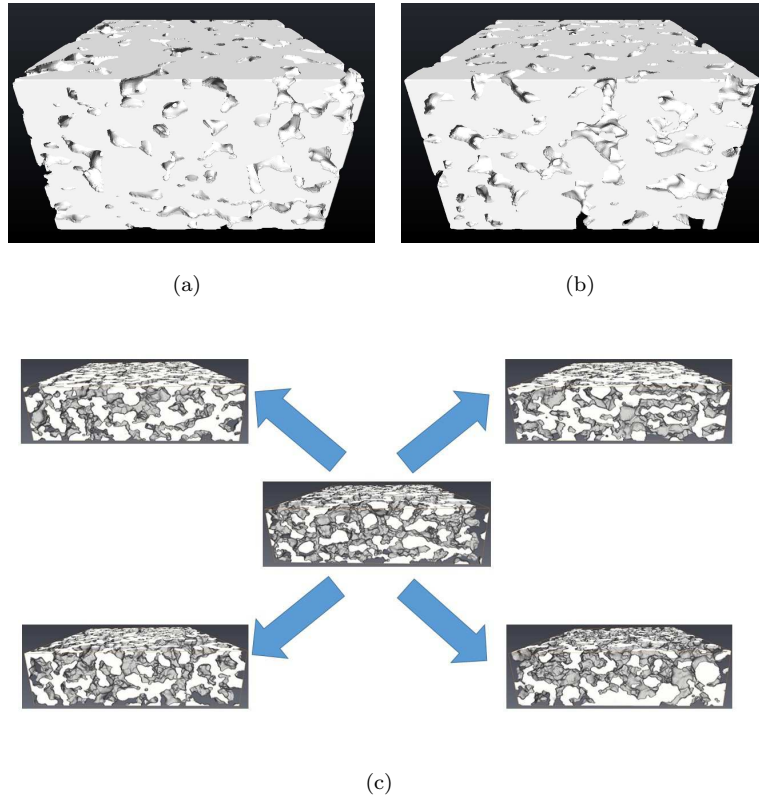


Figure 3: (a) 3D rendering of a cutout of a tomographic image of the energy cell anode. (b) 3D rendering of a simulated energy cell anode structure. (c) Realizations of the power cell model with various morphological properties; center: realization of the calibrated power cell model; top left: virtual structure with higher volume fraction of the particle phase; top right: virtual structure with more pronounced anisotropy effects; bottom left: virtual structure with no anisotropy effects; bottom right: virtual structure with decreasing volume fraction of the particle phase from bottom to top. Reprinted from [37](a+b) and [51](c) with permission from Elsevier.

270 *2.2. Microscopic cell modeling*

In this section we recollect the equations that describe the transport of lithium ions in a three-dimensional microstructure generated by the method as described in the previous section. The physical model has been derived based on species, charge and energy conservation to yield a set of equations that describe the spatial and temporal distribution of lithium ions, electrical potentials and

275

temperature [13, 58]. However, in order to fit to the isothermal plating model we neglect the effects of heat production here and consider an isothermal system where temperature enters as a constant model parameter.

For the purpose of this study we restrict ourselves to half-cell simulations, i.e. we consider a porous graphite electrode modeled by the discussed stochastic method against a lithium foil as counter-electrode. The simulation domains are connected with the external operation conditions through dedicated current collector phases on each electrode. The remaining space of the computational domain is filled with ion conductive electrolyte.

Within the graphite particles we have the following equations for lithium concentration c_{Gr} and electrical potential Φ_{Gr}

$$\partial_t c_{\text{Gr}} = -\nabla \cdot \mathbf{N}_{\text{Gr}} = -\nabla \cdot [-D_{\text{Gr}} \nabla c_{\text{Gr}}] , \quad (2.1)$$

$$0 = -\nabla \cdot \mathbf{j}_{\text{Gr}} = -\nabla \cdot [-\sigma_{\text{Gr}} \nabla \Phi_{\text{Gr}}] , \quad (2.2)$$

where D_{Gr} is the lithium diffusion coefficient and σ_{Gr} is the electrical conductivity of the material. The ion flux and electric current density are denoted by \mathbf{N}_{Gr} and \mathbf{j}_{Gr} , respectively. Also in the domains of the lithium foil and the current collectors electronic conduction is considered and hence (2.2) is also solved in these domains (with the respective conductivities of course). Since there is no intercalation and diffusion of ions neither in the lithium counter-electrode nor in the current collectors, (2.1) is only relevant for the graphite domain.

Within the electrolyte domain, lithium concentration c_{El} and electrochemical potential φ_{El} are coupled through

$$\partial_t c_{\text{El}} = -\nabla \cdot \mathbf{N}_{\text{El}} = -\nabla \cdot \left[-D_{\text{El}} \nabla c_{\text{El}} + \frac{t_+}{F} \mathbf{j}_{\text{El}} \right] , \quad (2.3)$$

$$0 = -\nabla \cdot \mathbf{j}_{\text{El}} = -\nabla \cdot \left[-\kappa_{\text{El}} \nabla \varphi_{\text{El}} - \kappa_{\text{El}} \frac{t_+ - 1}{F} \frac{\partial \mu}{\partial c_{\text{El}}} \nabla c_{\text{El}} \right] , \quad (2.4)$$

where t_+ is the transference number of lithium in the electrolyte, κ_{El} is the ionic conductivity of lithium inside the electrolyte and F is the Faraday constant. The derivative of the electrolyte chemical potential is given as

$$\frac{\partial \mu}{\partial c_{\text{El}}} = \frac{R \cdot T}{c_{\text{El}}} \cdot \left(1 + \frac{\partial \log f_+}{\partial \log c_{\text{El}}} \right), \quad (2.5)$$

with T denoting the temperature, R the gas constant and f_+ the activity coefficient.
 300

On the interfaces between the electrodes and electrolyte two types of reactions need to be considered: That is an intercalation reaction on the graphite side and a lithium deposition reaction on the counter-electrode side. The different phases (graphite, electrolyte and counter-electrode) are coupled via interface
 305 conditions

$$\begin{aligned} \mathbf{j}_{\text{El}} \cdot \mathbf{n}_{\text{So-El}} &= i_{\text{interface}}, \\ \mathbf{j}_{\text{So}} \cdot \mathbf{n}_{\text{So-El}} &= i_{\text{interface}}, \\ \mathbf{N}_{\text{El}} \cdot \mathbf{n}_{\text{So-El}} &= \frac{i_{\text{interface}}}{F}, \\ \mathbf{N}_{\text{So}} \cdot \mathbf{n}_{\text{So-El}} &= \frac{i_{\text{interface}}}{F}, \end{aligned} \quad (2.6)$$

with ‘‘So’’ (solid) being either graphite or metallic lithium. By convention the interface normal $\mathbf{n}_{\text{So-El}}$ points from solid into the electrolyte. These conditions express the continuity of the current and mass fluxes between the phases. The current flow through these interfaces depends on the corresponding reactions.
 310 The intercalation reaction is described by a Butler-Volmer-like expression [58]

$$\begin{aligned} i_{\text{interface}} &= i_{\text{Gr-El}} \\ &= 2 \cdot i_{\text{Gr-El}}^{00} \cdot \sqrt{c_{\text{Gr}} \cdot c_{\text{El}}} \cdot \sinh \left(\frac{F}{2 \cdot R \cdot T} \cdot \eta_{\text{Gr-El}} \right), \end{aligned} \quad (2.7)$$

where the overpotential is given by $\eta_{\text{Gr-El}} = \Phi_{\text{gr}} - U_0^{\text{Gr}} - \varphi_{\text{El}}$. The electrode’s open-circuit potential U_0^{Gr} is a concentration dependent material property. The rate constant $i_{\text{Gr-El}}^{00}$ depends on the lithium salt and the electrolyte composition. The transfer coefficients $\alpha_c + \alpha_a = 1$ of the intercalation reaction were
 315 assumed to be symmetrical ($\alpha_{a,c} = 0.5$). The form of (2.7) differs from the usual

Table 1: Overview of interface conditions between the different material domains for the ion fluxes N and current densities j . “cont.” mathematically means no interface but a continuous flux according to the transport equation. Between the graphite electrode and the lithium foil as counter electrode there is obviously no interface.

	graphite	electrolyte	lithium foil	current collector	plated lithium
graphite	cont.	(2.6),(2.7)	no interface	$N = 0, j = \text{cont.}$	$N = 0, j = \text{cont.}$
electrolyte	(2.6),(2.7)	cont.	(2.6),(2.8)	$N = -1, j = 0$	(2.6),(2.14)
lithium foil	no interface	(2.6),(2.8)	cont.	$N = 0, j = \text{cont.}$	no interface
current col.	$N = 0, j = \text{cont.}$	$N = 0, j = 0$	$N = 0, j = \text{cont.}$	cont.	$N = 0, j = \text{cont.}$
plated lithium	$N = 0, j = \text{cont.}$	(2.6),(2.14)	no interface	$N = 0, j = \text{cont.}$	cont.

Butler-Volmer expression by omitting the common $(c_{\text{Gr}}^{\text{max}} - c_{\text{Gr}})_a^\alpha$ term, since a rigorous thermodynamically consistent derivation does not in general yield this prefactor [58]. The Butler-Volmer model and the used exchange current include a relation between the potentials and the current flux. The exponential shape of the exchange current introduces highly pronounced non-linearities into the numerical system. The reaction at the counter-electrode is described by a simple exchange current, which minimizes the effect of the counter-electrode on the simulation results

$$i_{\text{interface}} = i_{\text{CE-EI}} = 2 \cdot i_{\text{CE-EI}}^{00} \cdot \sinh\left(\frac{F}{2 \cdot R \cdot T} \cdot \eta_{\text{CE-EI}}\right), \quad (2.8)$$

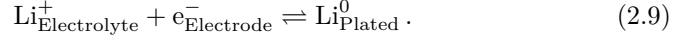
where the rate constant is given by $i_{\text{CE-EI}}^{00}$. On the lithium electrode the overpotential is simply given by $\eta_{\text{CE-EI}} = \Phi_{\text{CE}} - \varphi_{\text{EI}}$. The remaining interface conditions are shown in Tab. 1.

These equations describe an *ideal* battery, i.e. no degradation processes are considered. This extension is outlined in the next section.

2.3. Electrochemical degradation modeling

The focus in this work is the degradation process *lithium plating*, where the lithium ions form an unwanted metallic phase on the surface of the intercalation material of the negative electrode. The electrochemical modeling of this process is briefly described in the following section, details can be found in the

corresponding publication [29]. Two states of the lithium ions are of relevance:
 335 the lithium ions dissolved in the electrolyte Li_{El}^+ and the metallic/plated lithium
 phases Li_{Pl}^0 . The transition between these two is expressed by the reaction



The overpotential of the plating and stripping reaction is defined by the differ-
 ence between the electrochemical potential $\tilde{\mu}$ of the two lithium phases involved[59]

$$F \cdot \eta_{\text{Pl/St}} = \tilde{\mu}_{\text{Li}^+}^{\text{Pl}} - \tilde{\mu}_{\text{Li}^+}^{\text{El}}. \quad (2.10)$$

With the definition of the reference state $\mu_{\text{Li}^0}^{\text{Pl}} = \mu_{\text{Li}^+}^{\text{Pl}} + \mu_{e^-}^{\text{Pl}}$ and the electro-
 340 chemical potentials of lithium ions inside the electrolyte and a solid phase (see
 [29]), the overpotential (2.10) can be rewritten to

$$\eta_{\text{Pl/St}} = \Phi_{\text{Pl}} - \varphi_{\text{Li}^+}^{\text{El}}, \quad (2.11)$$

where φ_i^p denotes the electrochemical potential of species i in phase p with
 respect to the reference state $\mu_{\text{Li}^0}^{\text{Pl}}$. Plating of lithium is occurring if the overpot-
 ential reaches negative values ($\eta_{\text{Pl/St}} < 0$). The metallic lithium phase on the
 345 surface of the anode is not in a stable configuration, even if no external current
 is applied to the system. As soon as lithium is plated on the surface of the
 active material, the lithium metal can react with its surroundings in different
 ways. The reaction between the plated lithium and the electrolyte results in the
 growth of a solid-electrolyte interphase (SEI), which leads to an irreversible loss
 350 of lithium [22]. Apart from phenomenological models no theory exists which
 combines lithium intercalation, lithium plating and SEI growth. Hence, this
 irreversible pathway is not included in the present paper. The plated lithium
 can also intercalate charge-neutrally into the supporting graphite. This reaction
 represents a reversible lithium stripping pathway. We are not aware of any lit-
 355 erature regarding the identification and parameterization of the charge-neutral

reintercalation. Hence the direct reintercalation from the plated lithium into graphite was neglected in this work.

The stripping and plating reaction of the lithium is described by a Butler-Volmer-like equation

$$i_{\text{P1-E1}} = i_{\text{P1-E1}}^{00} \cdot \sqrt{c_{\text{E1}}} \cdot \left(f_{\text{pre}}(n_{\text{Li}}) \cdot \exp\left(\frac{F\eta_{\text{P1-E1}}}{2 \cdot R \cdot T}\right) - \exp\left(-\frac{F\eta_{\text{P1-E1}}}{2 \cdot R \cdot T}\right) \right). \quad (2.12)$$

360 The Butler-Volmer-like expression is derived for non-vanishing phases. But, the plated lithium phase can completely desolve during stripping. Hence, the vanishing of the plated lithium phase is considered in the exchange current by the numerical regularization function $f_{\text{pre}}(n_{\text{Li}})$, which depends on the amount of plated lithium n_{Li}

$$f_{\text{pre}}(n_{\text{Li}}) = \frac{(n_{\text{Li}})^4}{(n_{\text{Li}}^{\text{const}})^4 + (n_{\text{Li}})^4}. \quad (2.13)$$

365 Based on numerical considerations [29], we set the constant $n_{\text{Li}}^{\text{const}}$ to a value corresponding to a thickness of plated lithium of 0.48 nm. For partially covered surfaces more detailed models are necessary to capture the stripping of partially covered surfaces including the surface-driven dissolution of small lithium droplets.

370 At the interface between the plated lithium and the electrolyte the current through the interface is equal to the stripping current

$$i_{\text{interface}} = i_{\text{P1-E1}}. \quad (2.14)$$

All the interface conditions which are relevant for electrochemical simulations in this paper are listed in Tab. 1.

In this paper the stripping process of plated lithium is simulated by including 375 the plated lithium into the 3D microstructure as an additional volume phase. In

Fig. 4(a) an example of a 3D microstructure with plated lithium is shown. The porous electrode (red/right) is generated by the stochastic generation algorithm as described in Sec. 2.1. Additionally, regions with plated lithium are positioned randomly at the separator-electrode interface. The microstructure shown in Fig.

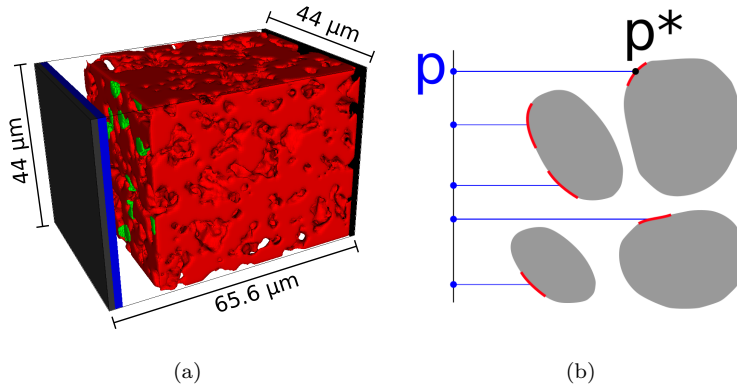


Figure 4: (a) Example of a 3D microstructure generated based on the stochastic simulation algorithm as described in Sec. 2.1. The plated lithium is shown as green spots on the separator-graphite interface. (b) Schematic depiction of the simulated initial lithium plating in 2D. The blue dots indicate the starting positions of the grains. The red lines indicate the simulated lithium plating.

380 4(a) is used for the model order reduction experiment described in Sec. 3.2.

One important deviation from the microstructure model [37, 51] was to introduce a third phase in the anode structure, plated lithium. We use a fairly simple model to create a slightly plated structure as initial condition. These initial conditions are, like the microstructure model, simulated stochastically. 385 This means that for every run the microstructure model extended by the plated lithium phase generates a new structure but with similar statistical properties.

The method used to create the plated lithium phase is a germ-grain model. This means that in a first step germs are simulated and in the second step grains are placed around the germs [31]. The parameters of this model are the intensity λ of the Poisson process that is used to generate the germs and the grain radius r_s . 390 Due to the lack of experimental data the values were chosen

to $\lambda = 0.01/\mu\text{m}^2$ and $r_s = 2.2\mu\text{m}$. The general idea of the model is to place plating germs randomly on the surface of the particles in the electrode and then initialize plating around the germs on all the points on the structure's surface within the radius given by r_s . In more detail the following is done, see Fig. 4(b):

- Select points $\{p_i, i \in \mathbb{N}\}$ at the separator-anode interface via a Poisson point process with intensity λ .
- For each point $p_i, i \in \mathbb{N}$ do the following:
 - Find the first point p_i^* where the straight line from p_i towards the anode current collector interface meets the anode structure. Let Θ be the particle on the boundary of which p_i^* is placed.
 - Consider a sphere $B(p_i^*, r_s)$ around p_i^* with radius r_s . Let $L_i = \{x \in \mathbb{R}^3 : x \in B(p_i^*, r_s) \text{ and } x \in \partial\Theta\}$, where $\partial\Theta$ is the boundary of Θ .
- Let $L = \bigcup_{i \in \mathbb{N}} L_i$ be the plated lithium phase.

The plated lithium phase L is then discretized as a one voxel thick phase on the surface of the particles. The material parameters and reaction constants of the ion transport and plating model are adapted from a previous publication [29].

2.4. Discretization and high-dimensional simulation

For the spatial discretization of the presented plating model, a cell-centered finite volume scheme on a uniform voxel grid is considered. Hence the discretization is naturally conservative. Furthermore, with the simple grid structure meshing of the complex microstructure is straight-forward. The Butler-Volmer interface conditions (2.6) are prescribed as the numerical flux across the respective domain interfaces, leading to a global space differential operator on the entire computational domain. Choosing implicit Euler time stepping for time discretization, we obtain a series of discrete nonlinear equation systems of the form

$$\begin{aligned} \begin{bmatrix} \frac{1}{\Delta t^{(n+1)}}(c_\mu^{(n+1)} - c_\mu^{(n)}) \\ 0 \end{bmatrix} + A_\mu \begin{pmatrix} c_\mu^{(n+1)} \\ \varphi_\mu^{(n+1)} \end{pmatrix} &= 0, \\ (c_\mu^{(n+1)}, \varphi_\mu^{(n+1)}) &\in V_h \oplus V_h. \end{aligned} \quad (2.15)$$

Here, V_h denotes the discrete finite volume space of locally constant grid functions, $c_\mu^{(n)}, \varphi_\mu^{(n)} \in V_h$ denote the concentration and potential fields at time step n for some p -tuple of model parameters μ contained in a parameter domain of interest $\mathcal{P} \subset \mathbb{R}^p$, and $A_\mu : V_h \oplus V_h \rightarrow V_h \oplus V_h$ is the finite volume space differential operator. The system is closed by $c_\mu^{(0)} = c_0$ for some fixed initial lithium distribution $c_0 \in V_h$. The time step size $\Delta t^{(n)}$ is chosen adaptively for each time step to accommodate the different time scales during and after the stripping of the plated lithium. The nonlinear equation systems are solved in BEST using Newton's method and an algebraic multigrid solver for the solution of the linear correction equations. Details on the discretization are provided in a previous publication [60].

2.5. Model order reduction and reduced simulation

The computation of a single solution trajectory $c_\mu^{(n)}, \varphi_\mu^{(n)}$ requires many hours, even for relatively small geometries (cf. Sec. 3.2). In order to make parameter studies computationally feasible, reduced basis model reduction techniques [61, 62, 63] are applied which have been implemented in our model order reduction library pyMOR [46, 47]. This allows us to obtain a quickly solvable reduced order model approximating the full order model (2.15).

To construct the reduced order model, solutions of (2.15) are computed for few appropriately selected parameters μ_1, \dots, μ_S . Various advanced algorithms exist for the selection of these *snapshot* parameters, often based on a greedy search procedure (cf. [61, 62, 63]). In our basic test case with a one-dimensional parameter domain \mathcal{P} (Sec. 3.2), a simple equidistant parameter sampling will be sufficient, however.

From this data, reduced approximation spaces $\tilde{V}_c, \tilde{V}_\varphi$ for the concentration and potential fields are constructed via proper orthogonal decomposition (POD, principal component analysis) [64] of the snapshot data sets $\mathcal{S}_c = \{c_{\mu_s}^{(n)}, c_{\mu_s}^{(n,i)}\}$, $\mathcal{S}_\varphi = \{\varphi_{\mu_s}^{(n)}, \varphi_{\mu_s}^{(n,i_k)}\}$. Here, $c_{\mu_s}^{(n,i)}, \varphi_{\mu_s}^{(n,i)}$ denote the intermediate Newton stages during the solution of (2.16), which are included for improved numerical stability. By construction, we in particular have $\tilde{V}_c \subseteq \text{span } \mathcal{S}_c$ and $\tilde{V}_\varphi \subseteq \text{span } \mathcal{S}_\varphi$. While $\dim V_h$ is in the order of 10^6 , we typically have $\dim \tilde{V}_c, \dim \tilde{V}_\varphi < 100$, which makes significant computational speedups possible.

After the reduced approximation space $\tilde{V} = \tilde{V}_c \oplus \tilde{V}_\varphi$ has been computed, the reduced order model is obtained via Galerkin projection of (2.15) onto \tilde{V} . I.e., we solve

$$P_{\tilde{V}} \left\{ \begin{bmatrix} \frac{1}{\Delta t^{(n+1)}} (\tilde{c}_\mu^{(n+1)} - \tilde{c}_\mu^{(n)}) \\ 0 \end{bmatrix} + A_\mu \left(\begin{bmatrix} \tilde{c}_\mu^{(n+1)} \\ \tilde{\varphi}_\mu^{(n+1)} \end{bmatrix} \right) \right\} = 0, \quad (\tilde{c}_\mu^{(n+1)}, \tilde{\varphi}_\mu^{(n+1)}) \in \tilde{V}, \quad (2.16)$$

$\tilde{c}_\mu^{(0)} = P_{\tilde{V}_c}(c_0)$, where $P_{\tilde{V}} / P_{\tilde{V}_c}$ denotes the L^2 -orthogonal projection onto \tilde{V} / \tilde{V}_c .

However, even though (2.16) contains only $\dim \tilde{V}$ degrees of freedom, its solution requires the evaluation of the high-dimensional system operator A_μ . This strongly limits the achievable speedup in computation time when solving (2.16) instead of (2.15).

To overcome this issue, A_μ is replaced by a quickly evaluable low-order approximation using the empirical interpolation technique [65, 66]: for an arbitrary (nonlinear) operator $O : X \rightarrow Y$, the EI-GREEDY algorithm is used to compute a low-order interpolation space $\tilde{Y} \subseteq Y$ from evaluations of T on given solution trajectories, after which the interpolated operator $\mathcal{I}_M[O]$ is determined by requiring it to agree with O at appropriate $M = \dim \tilde{Y}$ interpolation degrees of freedom $\pi_1, \dots, \pi_M : Y \rightarrow \mathbb{R}$. I.e., for all $x \in X$ we have

$$\mathcal{I}_M[O](x) \in \tilde{Y} \quad \text{and} \quad \pi_m(\mathcal{I}_M[O](x)) = \pi_m(O(x)), \quad 1 \leq m \leq M. \quad (2.17)$$

Due to the locality of finite volume operators, the point evaluations $\pi_m(O(x))$ can be computed quickly and independently from the dimension of V_h .

Since the potential part of A_μ vanishes identically for solutions of (2.15),
 470 a direct application of empirical interpolation to $O = A_\mu$ results in an unusable approximation, however. Instead, we further decompose A_μ and only use empirical interpolation for appropriate sub-operators.

In the following, we are interested in the behavior of the model in dependence on the applied current density. In this case, with μ being the applied current
 475 density, A_μ decomposes as

$$A_\mu = A_\mu^{(aff)} + A^{(bv)} + A^{(1/c)}, \quad (2.18)$$

where $A^{(bv)}$, $A^{(1/c)}$ are the parameter-independent nonlinear parts of A_μ corresponding to the Butler-Volmer interface terms and the summand in (2.4) containing $\partial\mu/\partial c_{El}$. Assuming constant t_+ , the remainder $A_\mu^{(aff)}$ is affine linear and decomposes as

$$A_\mu^{(aff)} = A^{(const)} + \mu \cdot A^{(bnd)} + A^{(lin)}, \quad (2.19)$$

480 where $A^{(const)}$ is constant and $A^{(bnd)}$, $A^{(lin)}$ are linear, non-parametric operators.

Now we apply the EI-GREEDY algorithm on the training datasets $\mathcal{S}_* = \{A^{(*)}(c_{\mu_s}^{(n)}, \varphi_{\mu_s}^{(n)}), A^{(*)}(c_{\mu_s}^{(n,i)}, \varphi_{\mu_s}^{(n,i)})\}$, $* \in \{bv, 1/c\}$, to obtain empirically interpolated operators $\mathcal{I}_{M^{(*)}}[A^{(*)}] \approx A^{(*)}$, which give us the approximation

$$A_\mu \approx \tilde{A}_\mu = A_\mu^{(aff)} + \mathcal{I}_{M^{(bv)}}[A^{(bv)}] + \mathcal{I}_{M^{(1/c)}}[A^{(1/c)}]. \quad (2.20)$$

485 Substituting (2.20) into (2.16) we arrive at the fully reduced model

$$P_{\tilde{V}} \left\{ \begin{bmatrix} \frac{1}{\Delta t^{(n+1)}} (\tilde{c}_\mu^{(n+1)} - \tilde{c}_\mu^{(n)}) \\ 0 \end{bmatrix} + \tilde{A}_\mu \left(\begin{bmatrix} \tilde{c}_\mu^{(n+1)} \\ \tilde{\varphi}_\mu^{(n+1)} \end{bmatrix} \right) \right\} = 0, \quad (\tilde{c}_\mu^{(n+1)}, \tilde{\varphi}_\mu^{(n+1)}) \in \tilde{V}, \quad (2.21)$$

with $\tilde{c}_\mu^{(0)} = P_{\tilde{V}_c}$. After pre-computation of the matrix representations of the linear (constant) operators $P_{\tilde{V}} \circ A^{(const)}, P_{\tilde{V}} \circ A^{(bnd)}, P_{\tilde{V}} \circ A^{(lin)} : \tilde{V} \rightarrow \tilde{V}$, as well as the projections from the interpolation spaces for $A^{(bv)}, A^{(1/c)}$ onto \tilde{V} , the solution of (2.21) can be obtained quickly for arbitrary new parameters μ with an effort that only depends on $\dim \tilde{V}$, $M^{(bv)}$ and $M^{(1/c)}$.

In the following experiments (see Sec. 3.2) we are interested in the cell potential as well as the average lithium concentration in the electrode as functions of time and the applied delithiation current density μ . These quantities are linear functionals $s_{cp}, s_{ac} : V_h \oplus V_h \rightarrow \mathbb{R}$, assigning to a state of the cell the respective quantity of interest. Due to their linearity, the vector representation for the evaluation of s_{cp}, s_{ac} on \tilde{V} can again be pre-computed, such that for any given solution of (2.21), $s_{cp}(\tilde{c}_\mu^{(n)}, \tilde{\varphi}_\mu^{(n)}), s_{ac}(\tilde{c}_\mu^{(n)}, \tilde{\varphi}_\mu^{(n)})$ are quickly obtained with an effort only depending on $\dim \tilde{V}$.

The model order reduction introduces an additional approximation error between full order and reduced order model that needs to be accounted for in the simulation workflow. As we are not aware of any rigorous error estimates which would provide sufficiently tight error bounds for the model under consideration, we here consider the following heuristic a posteriori error estimator [67]: In addition to \tilde{V} we construct a second, larger validation space $\hat{V} = \hat{V}_c \oplus \hat{V}_\varphi \supset \tilde{V}_c \oplus \tilde{V}_\varphi = \tilde{V}$ and extended interpolation bases of dimensions $\hat{M}^{(bv)} > M^{(bv)}$ and $\hat{M}^{(1/c)} > M^{(1/c)}$, yielding a larger reduced model with solutions $(\hat{c}_\mu^{(n)}, \hat{\varphi}_\mu^{(n)}) \in \hat{V}$. Under the heuristical assumption that

$$\|\hat{c}_\mu^{(n)} - c_\mu^{(n)}\| \leq \Theta \cdot \|\tilde{c}_\mu^{(n)} - c_\mu^{(n)}\|, \quad \|\hat{\varphi}_\mu^{(n)} - \varphi_\mu^{(n)}\| \leq \Theta \cdot \|\tilde{\varphi}_\mu^{(n)} - \varphi_\mu^{(n)}\| \quad (2.22)$$

for all timesteps n , $\mu \in \mathcal{P}$ with a fixed $\Theta \in [0, 1)$, from the triangle inequality we immediately obtain the error estimates

$$\|\tilde{c}_\mu^{(n)} - c_\mu^{(n)}\| \leq \frac{1}{1 - \Theta} \cdot \|\hat{c}_\mu^{(n)} - \tilde{c}_\mu^{(n)}\|, \quad \|\tilde{\varphi}_\mu^{(n)} - \varphi_\mu^{(n)}\| \leq \frac{1}{1 - \Theta} \cdot \|\hat{\varphi}_\mu^{(n)} - \tilde{\varphi}_\mu^{(n)}\|. \quad (2.23)$$

510 The right-hand sides of (2.23) can be quickly computed at the expense of an additional solution of a second (slightly larger) reduced order model. Note that (2.22) is precisely the *saturation assumption* in the context of hierarchical a posteriori estimates for finite element schemes (see e.g. [68]).

2.6. Algorithmical integration and software interfaces

515 MULTIBAT aims to allow computationally fast studies of local effects in the complex microstructure of battery anodes within one software workflow. This is achieved by breaking the multi-disciplinary goal into task units and interfacing these units with BEST to varying degrees of depth.

The presented workflow resulting from these interfaces is schematically depicted in Fig. 5. It allows speeding up the numerical solution of the microscopic cell degradation modeling from Sec. 2.2 and 2.3 with discretization from Sec. 2.4 by BEST, using the randomly generated structures from Sec. 2.1 through the POD/EI based model order reduction approach from Sec. 2.5. The workflow has been used to create the results and speedups depicted in Sec. 3.

525 We introduce three distinct interfaces. The first is file-based and allows usage of randomly generated structures of Sec. 2.1 in BEST through a conversion tool. The conversion tool provides standard BEST geometry input which is matched with physical modeling input parameters and numerical solution parameters suitable for the models of Sec. 2.2 with the extensions from Sec. 2.3.

530 The second interface allows to extend the BEST numerical solution code to advanced interface flux modeling between the plated anode-lithium and the electrolyte from Sec. 2.3. The model extensions are compiled into the BEST library.

The third and most extensive interface is library-based and gives pyMOR 535 runtime access to the solution process, vectors, discretization matrices, Jacobians, linear algebra solver and parameters of BEST through the BEST library to carry out POD/EI based MOR. The separation is strict: All MOR-related operations and the Newton methods are carried out in pyMOR and all evaluations of nonlinear operators and Jacobians are carried out by the BEST library

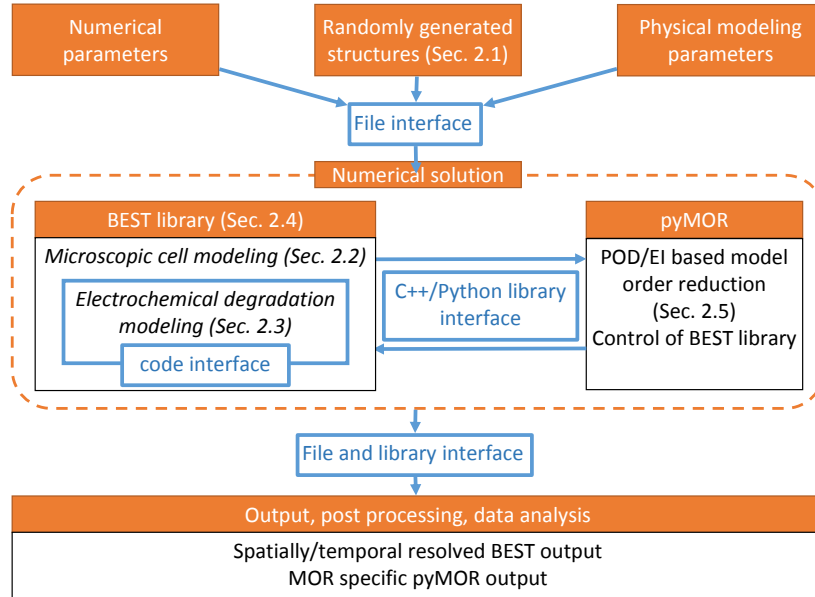


Figure 5: Implementation of the MULTIBAT workflow.

540 ordered by pyMOR.

3. Workflow demonstration on lithium stripping case study

3.1. Microstructure generation and electrochemical verification

The stochastic microstructure model used in this work was parameterized on real tomographic image data [37]. As mentioned in Sec. 2.1, the validity of the structural parameterization was investigated through spatially resolved electrochemical simulations [50]. The validated stochastic microstructure model is used in this work. In the following a short summary of the electrochemical validation is given. 20 simulated realizations of the stochastic microstructure model and 20 microstructure cutouts from the tomographic image data are used as electrode structure samples for electrochemical simulations. These microstructures are delithiated with a constant current. The simulation results were compared using various electrochemical quantities, such as local current density and lithium concentration. A very good agreement between the real and

virtual microstructures was found, see Fig. 6(a). The advantage of spatially re-
 555 solved electrochemical simulations is the access to localized inhomogeneities.
 The spatial distribution of the electrolyte concentration for two cutouts of real
 and virtual microstructures is shown as an example in Fig. 6(a).

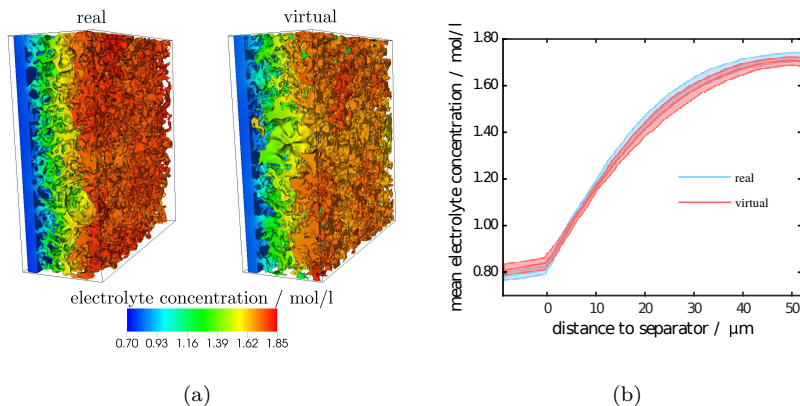


Figure 6: (a) Spatial distribution of electrolyte concentration of a real (left) and virtual (right) microstructure. The same color scale is used (shown below the cutouts). Both structures exhibit larger particles visible as void spaces. Also both cutouts show electrolyte pores, which are less connected to the main pore space: (virtual) Orange part close to the blue and (real) dark red at the upper corner. (b) Mean lithium concentration in the electrolyte as a function of the distance to the separator averaged over the different microstructures. The color shaded areas indicate the 5% and 95%-quantiles. A good accordance can be observed. Reprinted from [50] with permission from Elsevier.

Both cutouts exhibit similar features: less-than-average connected pores and large particles. Apart from the visual similarity between the real and virtual
 560 cutouts, averaged quantities were used for a more quantitative comparison. The average lithium concentration in the electrolyte in through direction (from one current collector towards the other) is shown in Fig. 6(b).

The general shapes of the concentration functions are nearly identical. The superposition of transport within the electrolyte and deintercalation of lithium
 565 from the solid phase results in a nonlinear gradient. Without any sources of lithium a linear concentration gradient forms in the separator. More details regarding the electrochemical validation can be found in the corresponding pub-

lication [50].

3.2. Model order reduction

570 As a first numerical test for the entire developed modeling and simulation workflow (see Sec. 2), we simulated the full model (including plated lithium) on a randomly generated half-cell geometry of size $44\mu\text{m} \times 44\mu\text{m} \times 65.6\mu\text{m}$, which is meshed with a grid of $100 \times 100 \times 149$ voxels (see Fig. 4(a)). This size is required to cover a representative volume containing several particles in each direction,
 575 and, at the same time, to achieve a sufficient resolution to resolve a relevant part of the electrode's morphology. Starting with plated lithium and a high lithium concentration in the electrode we performed a delithiation simulation and hence expect to see lithium stripping. We simulated 60 seconds with constant current densities in the interval $\mathcal{P} = [2.5, 250]\text{A}/\text{m}^2$, which corresponds to currents from
 580 4.84 nA to 484 nA or to C-rates from C/10 to 10C.

A single simulation of the full order model (2.15) requires around 16 hours (cf. Tab. 2). To generate the snapshot data for the computation of the reduced order model (2.21), the full order model (2.15) was solved for the three delithiation current densities $\min \mathcal{P}$, $\max \mathcal{P}$ and $(\min \mathcal{P} + \max \mathcal{P})/2$. The reduced spaces
 585 \tilde{V}_c , \tilde{V}_φ , \hat{V}_c , \hat{V}_φ , as well as the interpolation spaces for $\mathcal{I}_{M^{(bv)}}[A^{(bv)}]$, $\mathcal{I}_{M^{(1/c)}}[A^{(1/c)}]$ were computed using the POD and EI-GREEDY algorithms. To ensure that a numerically stable reduced order model is obtained, a small relative error tolerance of 10^{-7} was chosen, using in each case 97% of the resulting basis vectors for the construction of the reduced order model and all basis vectors for construction
 590 of the validation model used for the error estimator (2.23). The resulting spaces are of the following dimensions: $\dim \tilde{V}_c = 178$, $\dim \hat{V}_c = 183$, $\dim \tilde{V}_\varphi = 67$, $\dim \hat{V}_\varphi = 69$, $M^{(bv)} = 924$, $\hat{M}^{(bv)} = 952$, $M^{(1/c)} = 997$ and $\hat{M}^{(1/c)} = 1027$.

To validate the resulting reduced order model (2.21), we compared the solutions of (2.21) to the full order model (2.15) for 10 random parameter values
 595 $\mu_i \in \mathcal{P}$, $i = 1, \dots, 10$ in addition to the three snapshot parameters used for training. While achieving a relative model reduction error of at most $4.81 \cdot 10^{-4}$ resp. $4.50 \cdot 10^{-3}$ for the concentration and potential variables (Fig. 7), the reduced

order model can be simulated in less than 8 minutes, yielding a speedup factor of 120. Since the generation of the reduced model from the high-dimensional snapshot data is faster than a single solution of the full order model, an overall saving of computation time is already achieved for one additional model simulation (Tab. 2). For $\Theta = 0$ the error estimator (2.23) overestimates the real model reduction error in these 13 parameters by a factor of at most 1.08 (3.46) for the concentration (potential) and underestimates the error by a factor of at most 2.89 (1.45). The estimator was evaluated for 100 additional current densities in \mathcal{P} , yielding a maximum estimated relative error of $3.61 \cdot 10^{-4}$ resp. $5.55 \cdot 10^{-3}$ for concentration and potential.

In Fig. 8(a) and 8(b), the cell potential and average lithium concentration in the electrode have been plotted over the transferred charge for the 10 random test parameters. A short interpretation of these results is given in the subsequent section. Overall, no visual distinction between the data generated by the reduced and full order models can be made.

3.3. The lithium stripping process

In Fig. 8(a) the cell voltage is shown for 10 of the applied currents. The cell voltages for all applied currents exhibit a similar shape. A voltage plateau at the start of delithiation is followed by a rise, which is in turn succeeded by a region following the shape of the open-circuit potential U_0^{Graphite} . The initial voltage plateau results from the stripping reaction (see Eq. (2.9)). The increase in cell voltage begins as soon as the majority of the plated lithium is consumed. The apparent plateau afterwards is the cell voltage of the supporting graphite at about 75% state of charge. This equilibrium potential is shifted with an overpotential, which depends on the applied current. A transferred charge of 2 nAh corresponds to a variation in the state of charge of 4% since the used microstructure has a maximum capacity of 49 nAh. Large applied stripping currents lead to a fast decrease of lithium concentration at the surface of graphite. The solid diffusion can not equilibrate the lithium concentration in the electrode in the same rate for large currents as for small currents. Therefore,

Table 2: Extrapolated timings for the model reduction experiment. Time for single full model simulation: 15h 38m 35s (median), time for single reduced simulation: 7m 48s (median), time for generation of reduced model from snapshot data: 13h 43m 12s. ‘without MOR’ is the required time if all simulations are performed with the full order model (2.15), ‘with MOR’ is the required time if the reduced order model (2.21) is used for all simulations after the first 3 snapshot computations (including reduced order model construction). All computations have been performed on a single core of an Intel Xeon E5-2698 v3 CPU.

simulations	without MOR	with MOR	speedup
1	15h 38m	–	–
2	1d 7h 17m	–	–
3	1d 22h 55m	–	–
4	2d 14h 34m	2d 12h 46m	1.0
5	3d 6h 12m	2d 12h 54m	1.3
10	6d 12h 25m	2d 13h 33m	2.5
50	32d 14h 9m	2d 18h 45m	11.7
100	65d 4h 18m	3d 1h 15m	21.4
limit (= full model vs. reduced order model)			120.3

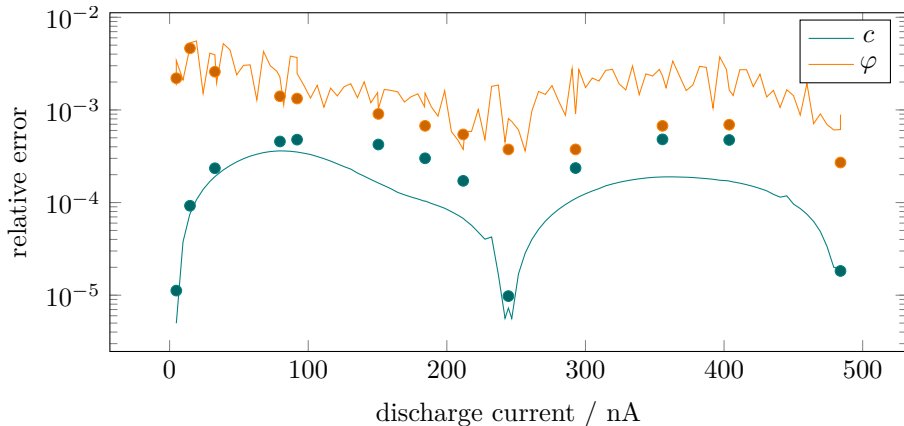
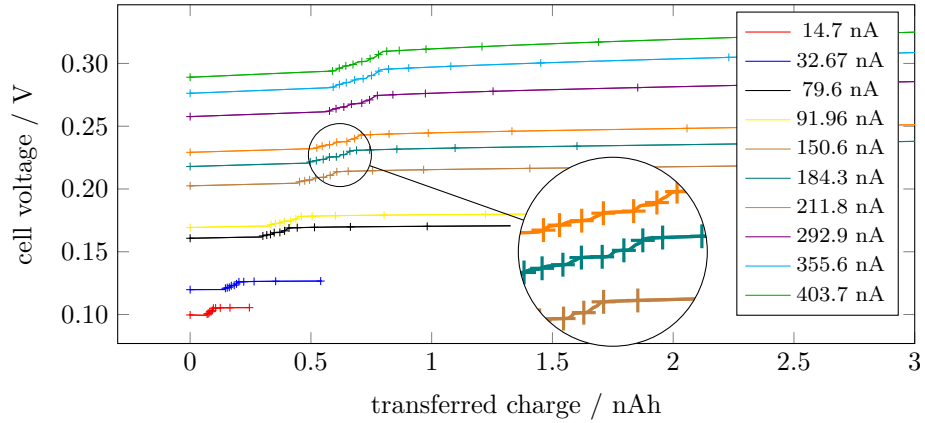


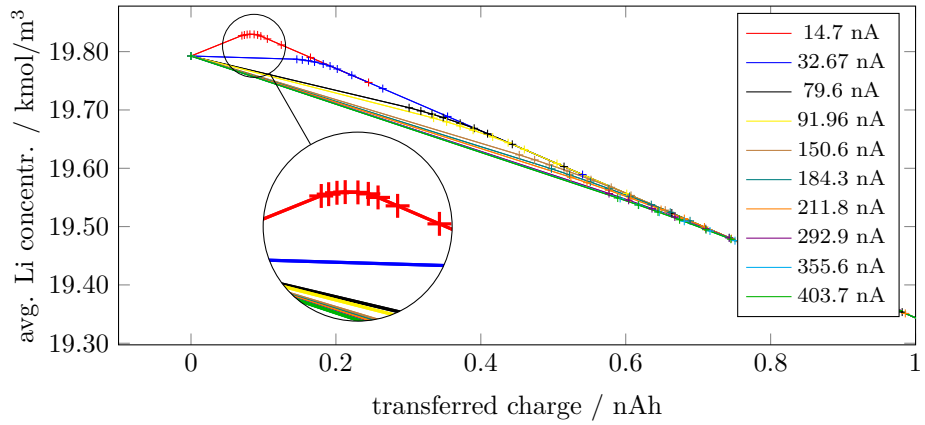
Figure 7: State space model reduction errors (markers) and estimated model reduction errors (solid lines) for different applied discharge current densities for the model reduction experiment. Plotted is the relative L^∞ -in-time L^2 -in-space error in the concentration (c) and potential (φ) variables over a test set of 10 randomly chosen current densities $\mu_i \in \mathcal{P} = [2.5, 250] \text{ A/m}^2, i = 1, \dots, 10$ in addition to the three current densities used for training of the reduced model. The model reduction error was estimated for additional 100 equidistantly sampled current densities in \mathcal{P} , $\Theta = 0$.

the state of charge at the surface will vary more than the overall change in state of charge. The open-circuit potential will then increase faster for larger currents. Thus resulting in a more sloped cell voltage for the larger currents. The length of the stripping plateau in the cell voltage depends on the applied current. For smaller currents, the change from constant potential to graphite dominated region is at lower transferred charge. The intercalation of lithium during the stripping of the plated lithium leads to an increase of the lithium concentration in the solid phase, as can be seen in Fig. 8(b). For low applied currents a net intercalation during the lithium stripping is visible. As soon as the majority of the plated lithium is dissolved a net delithiation exists. More information about the distribution of the delithiation current on the stripping and intercalation reaction are provided in a recent publication [29].

The cell voltages and average lithium concentrations obtained from the model reduction experiments are identical to the ones obtained from the full



(a)



(b)

Figure 8: (a) Cell voltage over transferred charge for the model reduction experiment for 10 randomly selected current densities μ_i (cf. Fig. 7). Solid lines: full model simulation, markers: reduced model simulation (every fifth time step marked). (b) Mean lithium concentration inside the solid phase plotted over transferred charge for the model reduction experiment for 10 randomly selected currents densities μ_i (cf. Fig. 7). Solid lines: full model simulation, markers: reduced model simulation (every fifth time step marked).

order model. This indicates that the reduced model sufficiently represents the electrochemical relevant regions in the simulation domain.

4. Conclusion & outlook

645 We conclude that it is absolutely possible to do a lot of in-depth research on lithium-ion cells virtually. In this work we have shown one approach to solve many of the existing problems using simulation techniques for the investigation in lithium-ion battery cells.

650 First, the limitation of 1D or pseudo 2D models which consider only averaged structural quantities and thus neglect all local effects can be overcome by switching to spatially resolved 3D models. Hence we presented a physics-based model that describes the cell's behavior on a microscopic scale and includes effects of lithium plating and stripping. Based on the software tool BEST the mathematical model was implemented and solved in a three-dimensional geometry.

660 Another current limitation is that the acquisition of tomographic 3D images as basis for simulations is costly and restricts the ability to simulate new structures that have not been produced experimentally. This limitation is overcome by the usage of a 3D stochastic microstructure model which has been implemented in the software library GEOSTOCH. Once the model is fitted to a material by the usage of tomographic 3D images it is possible to generate arbitrary many virtual cutouts with arbitrary sizes. By reasonable changes on the model parameters it is even possible to generate structures that have not been processed experimentally in order to investigate their properties and to test their performance.

670 Finally, a great problem of simulation-based parameter studies in particular including the plating/stripping behavior is the extensive simulation runtime. This problem is solved using model order reduction methods implemented in the software library pyMOR, which speed up the simulation of similar cycles significantly. Tab. 2 shows a speedup of factor 120 for the simulation of the

reduced model in comparison to a full order model simulation.

Overall we have shown that the combinations of all the methods described above work well in a demo scenario and can improve the accuracy of the geometry models, increase the computational speed considerably, and extended the
675 predictive power of the electrochemical battery models.

Acknowledgement

This work was partially funded by BMBF under grant numbers 05M13VUA, 05M13PMA, 05M13AMF and 05M13CLA in the programme “Mathematik für Innovationen in Industrie und Dienstleistungen”.

680 References

- [1] M. Doyle, T. F. Fuller, J. Newman, Modeling of galvanostatic charge and discharge of the lithium/polymer/insertion cell, *Journal of The Electrochemical Society* 140 (6) (1993) 1526–1533.
- [2] T. F. Fuller, M. Doyle, J. Newman, Simulation and optimization of the dual
685 lithium ion insertion cell, *Journal of The Electrochemical Society* 141 (1) (1994) 1–10.
- [3] J. Newman, K. E. Thomas, H. Hafezi, D. R. Wheeler, Modeling of lithium-ion batteries, *Journal of Power Sources* 119 (2003) 838–843.
- [4] J. Newman, K. E. Thomas-Alyea, *Electrochemical Systems*, Third Edition,
690 John Wiley & Sons, 2012.
- [5] S. Santhanagopalan, Q. Guo, P. Ramadass, R. E. White, Review of models for predicting the cycling performance of lithium ion batteries, *Journal of Power Sources* 156 (2) (2006) 620–628.
- [6] P. Arora, R. E. White, M. Doyle, Capacity fade mechanisms and side re-
695 actions in lithium-ion batteries, *Journal of The Electrochemical Society* 145 (10) (1998) 3647–3667.

- [7] J. Remmlinger, S. Tippmann, M. Buchholz, K. Dietmayer, Low-temperature charging of lithium-ion cells Part II: Model reduction and application, *Journal of Power Sources* 254 (2014) 268–276.
- 700 [8] S. Tippmann, D. Walper, B. Spier, W. G. Bessler, Low-temperature charging of lithium-ion cells. Part I: Electrochemical modeling and experimental investigation on degradation behavior, *Journal of Power Sources* 252 (2014) 305–316.
- [9] M. Doyle, J. Newman, A. S. Gozdz, C. N. Schmutz, J.-M. Tarascon, Comparison of modeling predictions with experimental data from plastic lithium ion cells, *Journal of The Electrochemical Society* 143 (6) (1996) 1890–1903.
- 705 [10] M. Ecker, S. Kabitz, I. Laresgoiti, D. U. Sauer, Parameterization of a physico-chemical model of a lithium-ion battery: II. model validation, *Journal of The Electrochemical Society* 162 (9) (2015) A1849–A1857.
- 710 [11] A. Latz, J. Zausch, Multiscale modeling of lithium ion batteries: Thermal aspects, *Beilstein J. Nanotechnol.* 6 (2015) 987–1007.
- [12] A. Latz, J. Zausch, Thermodynamic consistent transport theory of Li-ion batteries, *Journal of Power Sources* 196 (6) (2011) 3296–3302.
- [13] A. Latz, J. Zausch, O. Iliev, Modeling of species and charge transport in Li-ion batteries based on non-equilibrium thermodynamics, in: I. Dimov, S. Dimova, N. Kolkovska (Eds.), *Numerical Methods and Applications*, Vol. 6046 of *Lecture Notes in Computer Science*, Springer, 2011, pp. 329–337.
- 715 [14] M. Smith, R. E. García, Q. C. Horn, The effect of microstructure on the galvanostatic discharge of graphite anode electrodes in LiCoO₂-based rocking-chair rechargeable batteries, *Journal of The Electrochemical Society* 156 (11) (2009) A896–A904.
- 720 [15] G. B. Less, J. H. Seo, S. Han, A. M. Sastry, J. Zausch, A. Latz, S. Schmidt, C. Wieser, D. Kehrwald, S. Fell, Micro-scale modeling of Li-ion batteries:

- Parameterization and validation, *Journal of The Electrochemical Society* 159 (6) (2012) 697–704.
- 725 [16] C.-W. Wang, A. M. Sastry, Mesoscale modeling of a Li-ion polymer cell, *Journal of The Electrochemical Society* 154 (11) (2007) 1035–1047.
- [17] T. Hutzenlaub, S. Thiele, N. Paust, R. M. Spotnitz, R. Zengerle, C. Walchshofer, Three-dimensional electrochemical Li-ion battery modelling featuring a focused ion-beam/scanning electron microscopy based
730 three-phase reconstruction of a LiCoO₂ cathode, *Electrochimica Acta* 115 (2014) 131–139.
- [18] B. Yan, C. Lim, L. Yin, L. Zhu, Simulation of heat generation in a reconstructed LiCoO₂ cathode during galvanostatic discharge, *Electrochimica*
735 *Acta* 100 (2013) 171–179.
- [19] M. Taralov, V. Taralova, P. Popov, O. Iliev, A. Latz, J. Zausch, On 2D finite element simulation of a thermodynamically consistent Li-ion battery microscale model, in: A. Slavova (Ed.), *Mathematics in Industry*, Cambridge Scholars Publishing, Newcastle upon Tyne, 2014, pp. 148–161.
- 740 [20] T. Hofmann, R. Müller, H. Andrä, J. Zausch, Numerical simulation of phase separation in cathode materials of lithium ion batteries, *International Journal of Solids and Structures* 100-101 (2016) 456–469.
- [21] Fraunhofer ITWM, BEST – Battery and Electrochemistry Simulation Tool (2014).
745 URL www.itwm.fraunhofer.de/best
- [22] J. Vetter, P. Novak, M. R. Wagner, C. Veit, K.-C. Möller, J. O. Besenhard, M. Winter, M. Wohlfahrt-Mehrens, C. Vogler, A. Hammouche, Ageing mechanisms in lithium-ion batteries, *Journal of Power Sources* 147 (1) (2005) 269–281.
- 750 [23] J. Newman, W. Tiedemann, Porous-electrode theory with battery applications, *AIChE Journal* 21 (1) (1975) 25–41.

- [24] P. Arora, M. Doyle, R. E. White, Mathematical modeling of the lithium deposition overcharge reaction in lithium-ion batteries using carbon-based negative electrodes, *Journal of The Electrochemical Society* 146 (10) (1999) 3543–3553.
- 755
- [25] M. Tang, P. Albertus, J. Newman, Two-dimensional modeling of lithium deposition during cell charging, *Journal of The Electrochemical Society* 156 (5) (2009) 390–399.
- [26] N. Legrand, B. Knosp, P. Desprez, F. Lopicque, S. Raël, Physical characterization of the charging process of a Li-ion battery and prediction of Li plating by electrochemical modelling, *Journal of Power Sources* 245 (2014) 208–216.
- 760
- [27] C. Monroe, J. Newman, Dendrite growth in lithium/polymer systems a propagation model for liquid electrolytes under galvanostatic conditions, *Journal of The Electrochemical Society* 150 (10) (2003) 1377–1384.
- 765
- [28] R. Akolkar, Mathematical model of the dendritic growth during lithium electrodeposition, *Journal of Power Sources* 232 (2013) 23–28.
- [29] S. Hein, A. Latz, Influence of local lithium metal deposition in 3D microstructures on local and global behavior of Lithium-ion batteries, *Electrochimica Acta* 201 (2016) 354–365.
- 770
- [30] D. P. Finegan, M. Scheel, J. B. Robinson, B. Tjaden, M. D. Michiel, G. Hinds, D. J. L. Brett, P. R. Shearing, Investigating lithium-ion battery materials during overcharge-induced thermal runaway: an operando and multi-scale X-ray CT study, *Physical Chemistry Chemical Physics* 18 (2016) 30912–30919.
- 775
- [31] S. N. Chiu, D. Stoyan, W. S. Kendall, J. Mecke, *Stochastic Geometry and its Applications*, 3rd Edition, J. Wiley & Sons, 2013.

- 780 [32] J. Mayer, V. Schmidt, F. Schweiggert, A unified simulation framework for spatial stochastic models, *Simulation Modelling Practice and Theory* 12 (2004) 307–326.
- [33] O. Stenzel, L. Koster, R. Thiedmann, S. D. Oosterhout, R. A. J. Janssen, V. Schmidt, A new approach to model-based simulation of disordered polymer blend solar cells, *Advanced Functional Materials* 22 (2012) 1236–1244.
- 785 [34] G. Gaiselmann, M. Neumann, L. Holzer, T. Hocker, M. R. Prestat, V. Schmidt, Stochastic 3D modeling of LSC cathodes based on structural segmentation of FIB-SEM images, *Computational Materials Science* 67 (2013) 48–62.
- [35] D. Westhoff, J. J. van Franeker, T. Brereton, D. P. Kroese, R. A. J. Janssen, V. Schmidt, Stochastic modeling and predictive simulations for the microstructure of organic semiconductor films processed with different spin coating velocities, *Modelling and Simulation in Materials Science and Engineering* 23 (2015) 045003.
- 790 [36] M. Neumann, J. Stanek, O. Pecho, L. Holzer, V. Benes, V. Schmidt, Stochastic 3D modeling of complex three-phase microstructures in SOFC-electrodes with completely connected phases, *Computational Materials Science* 118 (2016) 353–364.
- 795 [37] J. Feinauer, T. Brereton, A. Spetl, M. Weber, I. Manke, V. Schmidt, Stochastic 3D modeling of the microstructure of lithium-ion battery anodes via Gaussian random fields on the sphere, *Computational Material Science* 109 (2015) 137–146.
- 800 [38] L. Cai, R. White, Reduction of model order based on proper orthogonal decomposition for lithium-ion battery simulations, *Journal of The Electrochemical Society* 156 (3) (2009) 154–161.
- [39] C. Long, R. E. White, Reduction of model order based on proper orthogonal

- 805 decomposition for lithium-ion battery simulations, *Journal of The Electrochemical Society* 156 (3) (2009) 154–161.
- [40] O. Iliev, A. Latz, J. Zausch, S. Zhang, On some model reduction approaches for simulations of processes in Li-ion battery., in: *Proceedings of Algoritmy 2012, conference on scientific computing*, Vysoké Tatry, Podbanské, 810 Slovakia, Slovak University of Technology in Bratislava, 2012, pp. 161–171.
- [41] A. Wesche, S. Volkwein, The reduced basis method applied to transport equations of a lithium-ion battery, *COMPEL: The International Journal for Computation and Mathematics in Electrical and Electronic Engineering* 32 (2013) 1760–1772.
- 815 [42] O. Lass, S. Volkwein, Parameter identification for nonlinear elliptic-parabolic systems with application in lithium-ion battery modeling, *Computational Optimization and Applications* 62 (1) (2015) 217–239.
- [43] M. Ohlberger, S. Rave, S. Schmidt, S. Zhang, A model reduction framework for efficient simulation of li-ion batteries, in: J. Fuhrmann, M. Ohlberger, 820 C. Rohde (Eds.), *Finite Volumes for Complex Applications VII-Elliptic, Parabolic and Hyperbolic Problems*, Vol. 78 of *Springer Proceedings in Mathematics & Statistics*, Springer International Publishing, 2014, pp. 695–702.
- [44] M. Ohlberger, S. Rave, F. Schindler, Model reduction for multiscale 825 lithium-ion battery simulation, in: B. Karasözen, M. Manguoğlu, M. Tezer-Sezgin, S. Göktepe, Ömür Uğur (Eds.), *Numerical Mathematics and Advanced Applications ENUMATH 2015*, Vol. 112 of *Lecture Notes in Computational Science and Engineering*, Springer, 2016, pp. 317–331.
- [45] M. Ohlberger, S. Rave, Localized reduced basis approximation of a non- 830 linear finite volume battery model with resolved electrode geometry, in: P. Benner, M. Ohlberger, A. Patera, G. Rozza, K. Urban (Eds.), *Model Reduction of Parametrized Systems*, no. 17 in *MS&A*, Springer International Publishing, 2017, pp. 201–212.

- [46] R. Milk, S. Rave, F. Schindler, pyMOR - Generic algorithms and interfaces
835 for model order reduction, *SIAM J. Sci. Comput.* 35 (5) (2016) 194–216.
- [47] pyMOR Developers and Contributors, pyMOR – Model Order Reduction
with Python (2013–2016).
URL www.pymor.org
- [48] O. Iliev, A. Latz, M. Ohlberger, S. Schmidt, V. Schmidt, The multibat
840 project (2016).
URL [https://wwwmath.uni-muenster.de/num/ohlberger/\research/
projects/MULTIBAT](https://wwwmath.uni-muenster.de/num/ohlberger/\research/projects/MULTIBAT)
- [49] G. Gaiselmann, R. Thiedmann, I. Manke, W. Lehnert, V. Schmidt,
Stochastic 3D modeling of fiber-based materials, *Computational Materi-
845 als Science* 59 (2012) 75–86.
- [50] S. Hein, J. Feinauer, D. Westhoff, I. Manke, V. Schmidt, A. Latz, Stochastic
microstructure modeling and electrochemical simulation of lithium-ion cell
anodes in 3D, *Journal of Power Sources* 336 (2016) 161–171.
- [51] D. Westhoff, J. Feinauer, K. Kuchler, T. Mitsch, I. Manke, S. Hein, A. Latz,
850 V. Schmidt, Parametric stochastic 3D model for the microstructure of an-
odes in lithium-ion power cells, *Computational Materials Science* 126 (2017)
453–467.
- [52] C. Lautensack, Random Laguerre tessellations, Ph.D. thesis, Universität
Karlsruhe (TH) (2007).
- 855 [53] J. Møller, Random tessellations in \mathbb{R}^d , *Advances in Applied Probability*
21 (1) (1989) 37–73.
- [54] S. Torquato, *Random Heterogeneous Materials: Microstructure and Macro-
scopic Properties*, Springer, 2002.
- [55] R. C. Prim, Shortest connection networks and some generalizations, *The
860 Bell System Technical Journal* 36 (6) (1957) 1389–1401.

- [56] A. Lang, C. Schwab, Isotropic Gaussian random fields on the sphere: regularity, fast simulation, and stochastic partial differential equations, *Annals of Applied Probability* 25 (6) (2015) 3047–3094.
- [57] E. Dougherty (Ed.), *Mathematical Morphology in Image Processing*, Optical Science and Engineering, Taylor & Francis, 1992.
- [58] A. Latz, J. Zausch, Thermodynamic derivation of a Butler–Volmer model for intercalation in Li-ion batteries, *Electrochim. Acta* 110 (2013) 358–362.
- [59] J. Newman, K. E. Thomas-Alyea, *Electrochemical systems*, 3rd Edition, J. Wiley & Sons, 2004.
- [60] P. Popov, Y. Vutov, S. Margenov, O. Iliev, Finite volume discretization of equations describing nonlinear diffusion in Li-ion batteries, *Numerical Methods and Applications* 6046 (2011) 338–346.
- [61] A. Quarteroni, A. Manzoni, F. Negri, *Reduced Basis Methods for Partial Differential Equations*, *La Matematica per il 3+2*, Springer International Publishing, 2016.
- [62] J. S. Hesthaven, G. Rozza, B. Stamm, *Certified Reduced Basis Methods for Parametrized Partial Differential Equations*, *SpringerBriefs in Mathematics*, Springer International Publishing, 2016.
- [63] B. Haasdonk, Reduced basis methods for parametrized pdes—a tutorial introduction for stationary and instationary problems, in: P. Benner, M. Ohlberger, A. Cohen, K. Willcox (Eds.), *Model Reduction and Approximation*, Society for Industrial and Applied Mathematics, 2017, Ch. 2, pp. 65–136.
- [64] L. Sirovich, Turbulence and the dynamics of coherent structures Part I: Coherent structures, *Quarterly of Applied Mathematics* 45 (3) (1987) 561–571.

- [65] M. Barrault, Y. Maday, N. C. Nguyen, A. T. Patera, An ‘empirical interpolation’ method: application to efficient reduced-basis discretization of partial differential equations, *Comptes Rendus Mathematique* 339 (9) (2004) 667–672.
- 890
- [66] M. Drohmann, B. Haasdonk, M. Ohlberger, Reduced basis approximation for nonlinear parametrized evolution equations based on empirical operator interpolation, *SIAM Journal on Scientific Computing* 34 (2) (2012) 937–969.
- 895
- [67] S. Hain, M. Ohlberger, M. Radic, K. Urban, A hierarchical a-posteriori error estimator for the reduced basis method, Working paper (under preparation) (2017+).
- [68] R. E. Bank, R. K. Smith, A posteriori error estimates based on hierarchical bases, *SIAM Journal on Numerical Analysis* 30 (4) (1993) 921–935.